Exp Fluids (2012) 52:1519–1532
DOI 10.1007/s00348-012-1268-6

RESEARCH ARTICLE

Proper orthogonal decomposition analysis for cycle-to-cycle variations of engine flow. Effect of a control device in an inlet pipe

Trung-Thanh Vu · Philippe Guibert

Received: 1 June 2011 / Revised: 7 December 2011 / Accepted: 18 January 2012 / Published online: 12 February 2012
© Springer-Verlag 2012

Abstract This paper aims to investigate cycle-to-cycle variations of non-reacting flow inside a motored single-cylinder transparent engine in order to judge the insertion amplitude of a control device able to displace linearly inside the inlet pipe. Three positions corresponding to three insertion amplitudes are implemented to modify the main aerodynamic properties from one cycle to the next. Numerous particle image velocimetry (PIV) two-dimensional velocity fields following cycle database are post-treated to discriminate specific contributions of the fluctuating flow. We performed a multiple snapshot proper orthogonal decomposition (POD) in the tumble plane of a pent roof SI engine. The analytical process consists of a triple decomposition for each instantaneous velocity field into three distinctive parts named mean part, coherent part and turbulent part. The 3rd- and 4th-centered statistical moments of the proper orthogonal decomposition (POD)-filtered velocity field as well as the probability density function of the PIV realizations proved that the POD extracts different behaviors of the flow. Especially, the cyclic variability is assumed to be contained essentially in the coherent part. Thus, the cycle-to-cycle variations of the engine flows might be provided from the corresponding POD temporal coefficients. It has been shown that the in-cylinder aerodynamic dispersions can be adapted and monitored by controlling the insertion depth of the control instrument inside the inlet pipe.

T.-T. Vu · P. Guibert (✉)
Institut Jean Le Rond d'Alembert, Université Pierre et Marie Curie, 2 Place de la Gare de Ceinture, 78210 Saint Cyr l'Ecole, France
e-mail: philippe.guibert@upmc.fr

Abbreviations

SI engine	Spark ignition engine
PIV	Particle image velocimetry
POD	Proper orthogonal decomposition
POD-MS	Multiple snapshot POD
IC	Internal combustion
IGR	Internal gas recirculation
EGR	Exhaust gas recirculation
CAD	Crank angle degree
ATDC or BTDC	After top dead center or before top dead center
IVO or IVC	Inlet valve opening or closing
EVO or EVC	Exhaust valve opening or closing
Nd-YAG laser	Neodymium-Yttrium Aluminum Garnet laser
CCD camera	Charge Couple Device camera
S_k ($K = 1\ldots3$) or S1	S2, S3, insertion depths of the control flap
X_m	Spatial variables corresponding to one node point
t_i	Temporal variables corresponding to the ith cycle
$\vec{U}$	Two-dimensional PIV velocity vector
U_1 or U_2	Horizontal or vertical component
$a^{(n)}$ (S_k, t_i)	nth POD mode for S_k at cycle t_i
$\lambda^{(n)}$	Eigenvalue of the nth POD mode
$\Phi_1^{(n)}(X_m)$ or $\Phi_2^{(n)}(X_m)$	Eigenvectors of mode n at X_m relative to U_1 or U_2
U'	Velocity component of a homogeneous isotropic turbulent flow
$S_{U'}$	Skewness or 3rd-centered statistical moment of U'

$F_{U'}$	Flatness or 4th-centered statistical moment of U'
E	Total kinetic energy

1 Introduction

One of the most important targets of the in-cylinder flow control is to reduce the dispersions between the engine cycles. Favorable aerodynamics to combustion process being expected in order to decrease exhaust pollutant emissions and optimize engine efficiency, a satisfactory cyclic reproducibility is highly required. A variety of researches have been stimulated by the above motivation to further understand the vortex motion behaviors and evaluate the cycle-to-cycle variations (Towers and Towers 2004; Guibert and Le Moyne 2002; Rempfer and Fasel 1994; Matekunas 1983; Young 1981; Enotiadis et al. 1990). As demonstrated by these works, the cyclic variability is directly linked to turbulence, pressure variations at inlet and exhaust strokes, acoustics phenomena in pipes, mixing process induced modified thermodynamic evolution, local equivalence ratio, flame velocity, heat transfer, quenching, IGR and EGR quantity… All mentioned features are inter-dependent and have great impacts on the ignition and the development of the turbulent flame. In particular, the instability of the coherent structures (Brown and Roshko 1974; Hussain 1986; Lumley 1967; Berkooz 1991) that contain mainly the kinetic energy seems to be the major actor of the cycle-to-cycle variations. According to Heywood (1988), the vortex created at intake stroke undergoes compression and breakdowns into small-scale structures before ignition. The vortex generating and breaking processes are influenced by engine design (Eichenberger and Robert 1999; Han and Reitz 1995; Kuwahara and Ando 2000; Huang et al. 2009; Huang et al. 2008). Successively, the intensity of the turbulence affects locally and heavily the propagating speed of the flame traveling across the combustion chamber (Tabaczinski 1990). As remarked in Druault et al. (2005), the large-scale organized fluid motions and the turbulence vary significantly from one engine cycle to the next. Consequently, the engines are less efficient than they might be due to the fact that the combustion process initiates from different conditions.

Aiming to prepare an in-cylinder aerodynamics with reduced cyclic dispersions, a relevant solution of intake port geometry modification was proposed by implementing charge motion control valves far upstream of the intake valves (Floch et al. 1995; Isaka and Higaki 1995; Zhongchang et al. 2002; Jebamani and Kumar 2008) or air jets and flaps in the pipe near the intake valves. As described in Stansfield et al. (2007) for SI engines, a tumble (a rotational fluid motion with an axis perpendicular to the cylinder axis) is generated at the intake stroke by the upper jet coming from the intake port. Meanwhile, the lower jet descends along the cylinder wall to result a recirculation zone. This recirculation zone might perturb the principle fluid structure and therefore increase the cyclic variability. The authors expected to promote the tumble development and decrease the influences of the recirculation zone by controlling both upper and lower jets. The engine performance and the volumetric efficiency are still preserved thanks to the control instrument minimization.

In the current work, the strategy implemented was proposed by Lenglet (2006). A flap is placed in the intake port near the inlet valve and can be linearly displaced. The control facility generates a small upstream perturbation, which in turn modifies the downstream flow field (refer to Fig. 1). At each CAD and for each fixed insertion depth of the control flap, the PIV measurements were performed on the tumble plane during 250 consecutive engine cycles. The PIV technique is now a well-established optical measurement method achieved by many relevant scientists to study the engine flow behaviors (Fansler 1993; Reeves et al. 1994, 1996, 1999; Reuss et al. 1989; Westerweel 1997). We recorded the resulting two-dimensional velocity fields and then analyzed them by the POD.

In regard to the POD, the method first introduced for fluid mechanics by Lumley (1967) is actually considered as

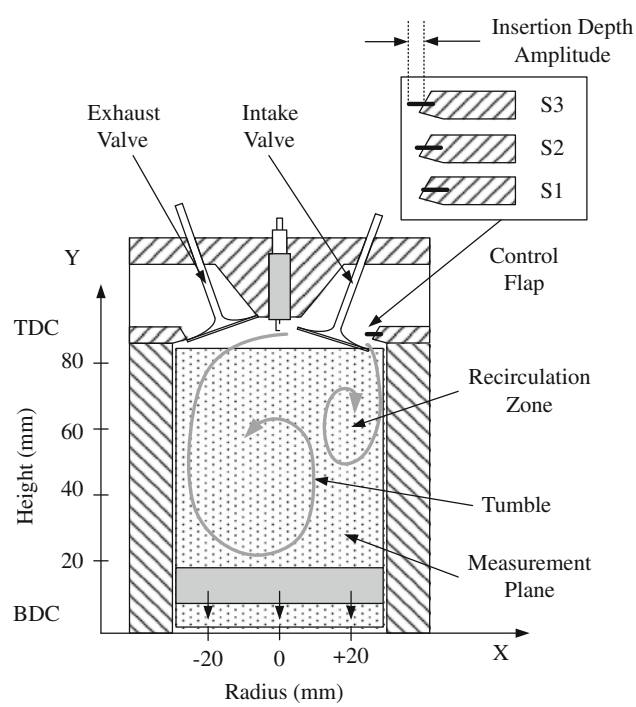

Fig. 1 Schematic (*not in scale*) of the flap placed in the intake port and location of the PIV measurement plane coinciding with the tumble plane

a powerful mathematical tool. According to Lumley (1967), a coherent structure has the largest mean square projection of the velocity field. The essential idea of the POD is finding among a set of realizations of the flow fields the one that maximizes the mean square energy. The method has been intensively investigated for real-time flow control and physical process simulation because of its ability to yield a basis for low-order dynamic systems (Berkooz 1991; Ly and Tran 2001; Utturkar et al. 2005; Rowley et al. 2004; Ravindran 2002; Epureanu 2003; Perret et al. 2006), and especially for the cyclic variability evaluation via statistical properties of the POD temporal coefficients (Druault et al. 2005; Druault and Chaillou 2007; Roudnitzky et al. 2006; Cosadia et al. 2006; Bizon et al. 2010; Fogleman et al. 2004; Graftieaux et al. 2001).

The paper is organized as follows. At first in Sect. 2, the experimental setup of the measured data is outlined. Section 3 then reviews the theoretical features of the POD and presents concretely the multiple snapshot POD used. The analysis of the cycle-to-cycle variations and the evaluation of the insertion depth of the control instrument are focused on in Sect. 4. The article is ended by several conclusions and perspectives.

2 Experimental setup

2.1 Model engine

The model engine is built using a transparent cylinder, which offers some wide optical accesses prior to the PIV measurement of the aerodynamic fields inside the combustion chamber. The cylinder head has two intake valves, two exhaust valves and a pent roof. The engine with a flat piston is driven at 1,200 rpm without firing. One cycle duration is 0.1 s, which corresponds to a frequency of 10 Hz. Refer to Table 1 for the engine specifications.

Table 1 Engine specifications

Engine characteristics	Value
Compression ratio	8.5:1
Inlet valve diameter	27.1 mm
Exhaust valve diameter	24.4 mm
Displacement	349 cm^3
Cylinder bore	75 mm
Stroke	79 mm
IVO	−15-CAD
IVC	210-CAD
EVO	−200-CAD
EVC	15-CAD

A control flap is located 20 mm upstream the inlet valve and can be moved linearly inside the inlet pipe. Three cases of insertion depth of the control flap called S1, S2 and S3 are tested. The perturbation is generated by plate protrusion from 0 mm for S1 to 3 mm for S3 (Fig. 1), allowing a slightly intrusive control.

2.2 PIV measuring system

The tracer particles (silicon oil droplets of approximately 1 μm diameter) are introduced in the intake plenum and illuminated by a light sheet of less than 1 mm thickness emitted from a double-pulsed Nd-YAG laser (Spectra Physics PIV 200 with a wavelength of 532 nm). The droplet size was measured by the phase Doppler anemometry (PDA) method. The scattered light is captured by a CCD camera (Dantec Flowsence 2 M, 8 bits) with a resolution of 1,600 × 1,186 pixels (height × width). The output energy at a wavelength of 532 nm is in the range of 120–140 mJ per pulse, with pulse duration of 12 ns. The frequency of the pulses is 10 ± 0.6 Hz allowing cycle-to-cycle continuous acquisition. The double-exposure imaging is realized through the transparent cylinder with a camera focused on the tumble geometric plane (plane containing the cylinder axis passing between the two intake valves in Fig. 1). The spatial resolution is about 56 μm/pixel.

At each CAD and for each fixed insertion depth (see Fig. 1), the PIV measurements were performed on the tumble plane. For example, for the first flap position (S1) at 90-CAD ATDC, 250 consecutive PIV snapshots corresponding to 250 consecutive engine cycles were obtained. This procedure is carried out every 10 CAD from 90-CAD ATDC to 280-CAD ATDC for three flap insertion depths.

During the processing of the PIV images, the average displacement of the particles is first calculated using a cross-correlation algorithm with an interrogation window of 32 × 32 pixels and an overlap of 50%. Then, an interpolation based on the 3 × 3 neighbors replaces a small number of false vectors (0.5%). For each instantaneous velocity field, 99 × 73 instantaneous velocity vectors are finally provided with a spatial resolution of 0.896 mm.

2.3 Cyclic dispersions of flow fields

The field of view represents roughly the whole tumble plane surface inside the combustion chamber. In Fig. 2, six instantaneous velocity fields at different instants (cycles) t_i with $i = 1\ldots6$ corresponding to six consecutive engine cycles taken by the PIV measurement for the first flap position (S1) at 250-CAD ATDC are presented. The gray level representing the velocity amplitude (m/s) is superposed by the two-dimensional streamlines allowing observation of the fluid motions existing within the cylinder.

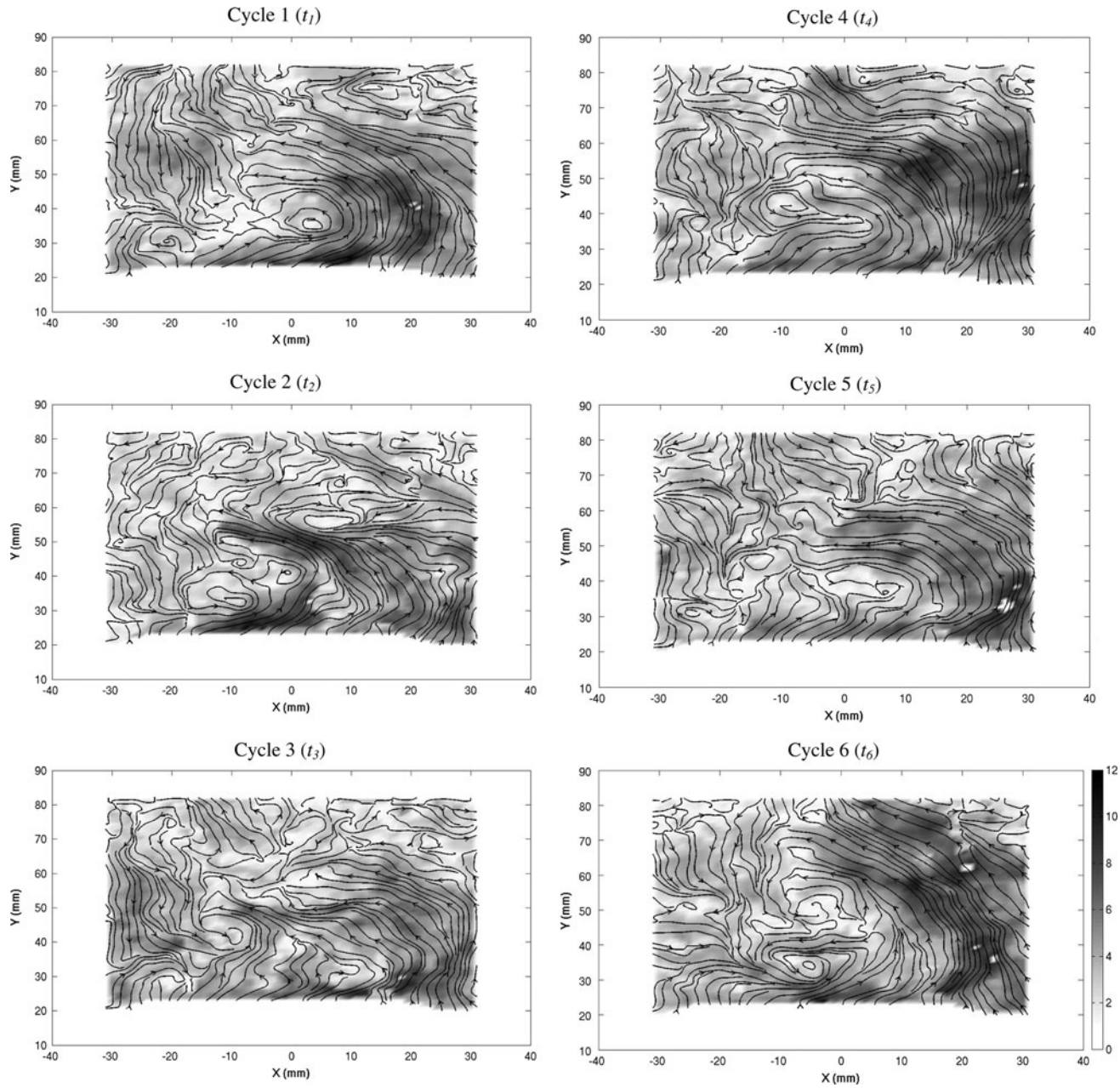

Fig. 2 Cycle-to-cycle variations of the flow fields for S1 at 250-CAD

At the beginning of the compression stroke, both upper and lower jets coming from the intake port are vanished and there is apparently no effect of admission existing in the velocity fields. In contrast, the piston (at the bottom of the images) moves upwards to break the large-scale structures to generate the turbulence. The dynamics of the piston have important impacts on the engine flow forcing an air motion on the right hand side at the bottom of the images. As the tumble rotates in a counter-clockwise direction, the piston enhances largely the air motion of the right hand side, which has an upward flow direction similar to the piston movement. Inversely, the air motion at the left hand side having a downward flow direction is prevented or even broken by the piston ascension. Especially, the behaviors of the tumble motions are different between the consecutive cycles in terms of morphology, position and intensity. Consequently, the turbulence generated from its breaking process varies significantly cycle by cycle. These cyclic dispersions are the major factors decreasing the engine performance since the combustion is initiated from different aerodynamic conditions.

3 Proper orthogonal decomposition

The POD has already been introduced by the formulas proposed in the literature. One can refer to Druault et al. (2005), Sirovich (1987), Holmes et al. (1998), Berkooz et al. (1993), Lumley (1967) for a detailed methodology. In this study, the snapshot POD (Sirovich 1987) is convenient and will be investigated because the number of collected samples is smaller than the space discretization. A phase-dependent multiple snapshot POD carried out at each CAD called POD-MS integrates simultaneously three control device positions (S1, S2 and S3) in the same database. Consequently, all flap positions have an identical POD eigenfunctions at each CAD. In contrast, different POD temporal coefficients are distributed depending on the control facility positioning. Therefore, an evaluation of the insertion depth of the control instrument in terms of cycle-to-cycle variations might be expected by comparing S1, S2 and S3. Note that no information of phase resolution within an engine cycle would be provided because the POD-MS considers separately the crank angle degrees. The POD-MS method applied for two-dimensional velocity vector PIV database is briefly described by the following subsections.

3.1 Analysis

At a given θ-CAD [θ-CAD takes one value of 90-CAD, 100-CAD, 110-CAD … 280-CAD], each flap position S_k has a set of $N_t = 250$ two-dimensional PIV snapshots expressed by a matrix function $\vec{U}(S_k, X_m, t_i)$ where S_k ($K = 1\ldots N_s$) is the insertion depth considered, $N_s = 3$ number of the control flap positions (S1, S2 and S3), X_m ($m = 1\ldots N_m$) is the space variables signifying the node points of the PIV mesh, $N_m = 99 \times 73$ is the total number of node points of the PIV mesh, t_i ($i = 1\ldots N_t$) is the ith engine cycle.

The POD-MS applied at θ-CAD is started by considering the instantaneous velocity field taken for the insertion depth S_k at engine cycles t_i and the one for S_h at t_j. The velocity correlation tensor is defined by:

$$R\big((S_k,t_i);(S_h,t_j)\big) = \frac{1}{N_m}\sum_{m=1}^{N_m} U_c(S_k,X_m,t_i)U_c\big(S_h,X_m,t_j\big) \qquad (1)$$

where $c = 1$ and $c = 2$ correspond, respectively, to the horizontal and the vertical velocity components ($Nc = 2$ is the total number of velocity components taken into account). The expression illustrates clearly that the POD-MS is a snapshot POD carried out at θ-CAD, except its cumulative set of snapshots including the realizations of S1, S2 and S3 in one unique database.

Let us get in detail the POD-MS at a concrete θ-CAD. Figure 3 shows the construction of the velocity matrix that

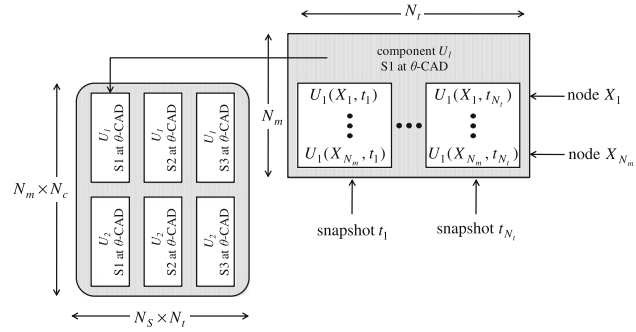

Fig. 3 Construction of the velocity matrix of the POD-MS carried out at θ-CAD

serves in the calculation of the velocity correlation tensor above. A $N_m \times N_t$ matrix cumulating all snapshots of horizontal velocity component U_1 for flap position S_1 at θ-CAD, that is, U_1 (S_1, X_m, t_i) is built-up and then contributes to the matrix. The procedure is similar for the vertical velocity component U_2. As seen in Fig. 3, two features are simultaneously integrated in the velocity matrix: the insertion depths and the engine cycles referenced, respectively, by S_k ($K = 1\ldots N_s$) and t_i ($i = 1\ldots N_t$).

Next, the Fredholm integral eigenvalue problem is computed from the velocity correlation matrix R to deduce a discrete series of POD temporal coefficients contained in matrix A and their corresponding POD eigenvalues$\lambda^{(n)}$:

$$RA^{(n)} = \lambda^{(n)}A^{(n)} \qquad (2)$$

with $A^{(n)} = \big(a^{(n)}(S_1,t_1),\ldots,a^{(n)}(S_1,t_{N_t}),\ a^{(n)}(S_2,t_1),\ldots,a^{(n)}(S_2,t_{N_t}),a^{(n)}(S_3,t_1),\ldots,a^{(n)}(S_3,t_{N_t})\big)$ as the nth POD temporal coefficients. One can find out that $A^{(n)}$ is a vector containing $N_n = N_t \times N_S = 250 \times 3 = 750$ elements and is able to supply the information about the flap positions (referenced by S_k with $K = 1\ldots3$) as well as the aerodynamic dispersions at θ-CAD between the engine cycles (referenced by t_i with $i = 1\ldots250$). In addition, the number of POD modes is $N_n = N_t \times N_S = 250 \times 3 = 750$.

For the sake of clarity, let us illustrate the arrangement of the matrix synthesizing the ensemble POD temporal coefficients at θ-CAD by Fig. 4. This matrix is constructed by placing side by side the vectors of POD temporal coefficients $A^{(n)}$ with $n = 1\ldots N_n$. The impact of the insertion depths of the control flap at θ-CAD can be underlined thanks to the structure of the matrix. Each column corresponds to $A^{(n)}$ relating to the nth POD mode. The first region that consists of first N_t lines represents the snapshots of the flap position S1 at θ-CAD. The flap positions S2 and S3 own the two next same-sized areas.

The POD-MS at θ-CAD is ended by calculating the nth POD eigenfunctions relative to the velocity component U_c, which is determined by projecting this component onto the POD temporal coefficients:

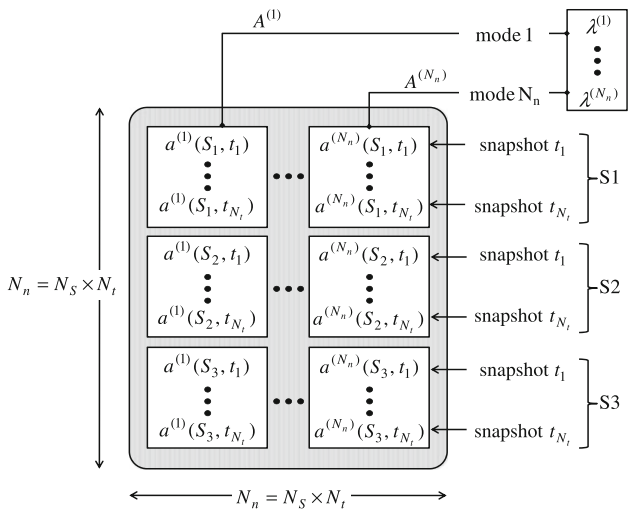

Fig. 4 Matrix including all POD temporal coefficients at one CAD

$$\Phi_c^{(n)}(X_m) = \sum_{k=1}^{N_S}\sum_{i=1}^{N_t} a^{(n)}(S_k,t_i)U_c(S_k,X_m,t_i) \tag{3}$$

In contrast with the POD temporal coefficients, the eigenfunctions $\vec{\Phi}^{(n)} = (\Phi_1^{(n)}, \Phi_2^{(n)})$ depend solely on the mesh point and therefore allow spatial specifications. We insist that the cycle-to-cycle dispersions given by the POD temporal coefficients and the effects of the insertion depths of the control flap are possibly obtained because the corresponding POD eigenfunctions are guaranteed to be identical for all three flap positions at one CAD considered.

3.2 Synthesis

In the previous subsection, the phase-dependent POD-MS is performed at θ-CAD. The velocity fields at θ-CAD depend on the space variable, the time variable and the insertion depth of the control device. Thus, the components of the velocity fields at θ-CAD are reconstructed as a linear combination of the POD modes. This procedure is done without difficulty knowing the structure of the matrix containing the POD temporal coefficients (Fig. 4):

$$U_c(S_k,\ X_m,\ t_i) = \sum_{n=1}^{N_n} a^{(n)}(S_k,\ t_i)\Phi_c^{(n)}(X_m) \tag{4}$$

Such reconstruction keeps the same total velocity field when the ensemble of eigenmodes is included in the formula. It is well known that a good approximation of the velocity fields is expected by using the first dominant modes in which the kinetic energy of the flow is concentrated. Additionally, the equation confirms the dependence of the velocity fields on the POD temporal coefficients and the POD eigenfunctions. As mentioned before, the cycle-to-cycle variations of the flow fields impacted by different insertion depths of the control flap can be studied via the POD temporal coefficients $a^{(n)}(S_k,t_i)$ since the POD eigenfunctions $\Phi_c^{(n)}(X_m)$ are identical for three flap positions. Such interesting property of the POD-MS permits an analysis of the cyclic variability, which will be presented in the following section.

4 Cycle-to-cycle variation analysis

The cyclic dispersions of the in-cylinder flows impact greatly the process generating turbulence and the combustion efficiency. Particularly, the cycle-to-cycle variations of the tumble are the major factor of such aerodynamic variability and therefore are solely focused on. We aim essentially to recommend which flap position among S1, S2 and S3 gives the less cycle-to-cycle variations. In order to distinguish the cyclic variability levels of the tumble motion influenced by the insertion depths, the POD triple decomposition (Roudnitzky et al. 2006; Druault et al. 2005) would be useful because it allows us to divide each instantaneous flow into three parts representing distinctive features. The mean part is associated with the most energetic vortex and therefore the average velocity field. The coherent part describes the cyclic variability of the vortex motions. The turbulent part links to the turbulent small-scale structures. Expecting to evaluate the impacts of the insertion depths on the cycle-to-cycle variations, we carry out at first a POD triple decomposition and then compare the coherent parts corresponding to S1, S2 and S3.

4.1 POD triple decomposition

The POD triple decomposition divides each instantaneous velocity field into three parts via the following expressions. Note that the sum of the coherent and turbulent parts is obviously the fluctuation part of the flow field.

The mean part covers the most energetic modes $(1 \div M)$ and represents the average flow. The cycle-to-cycle variations are described by the coherent part, which is reconstructed by the intermediate modes $(M+1 \div C)$ and contains mainly the fluctuating energy. The less energetic modes $(C+1 \div N_n)$ are contributed to the turbulent part for the small-scale fluid structures.

$$\begin{aligned} U(X,t) &= \underbrace{U^M(X,t)}_{\text{mean part}} + \underbrace{U^F(X,t)}_{\text{fluctuation part}} \\ &= \underbrace{U^M(X,t)}_{\text{mean part}} + \underbrace{U^C(X,t)}_{\text{coherent part}} + \underbrace{U^T(X,t)}_{\text{turbulent part}} \end{aligned} \tag{5}$$

$$U^M(X,t) = \sum_{n=1}^{M} a^{(n)}(t)\Phi^{(n)}(X) \tag{6}$$

$$U^C(X,t) = \sum_{n=M+1}^{C} a^{(n)}(t)\Phi^{(n)}(X) \tag{7}$$

$$U^T(X,t) = \sum_{n=C+1}^{N_n} a^{(n)}(t)\Phi^{(n)}(X) \tag{8}$$

In fact, the decomposition of the engine flow into three parts involves the determination of the cutoff modes M and C appearing in the above equations. These cutoff modes may be different depending on the crank angle degrees and the insertion depths. The separation between the mean and fluctuation parts, that is, choosing M, and the separation between the coherent and turbulent parts, that is, choosing C, are successively presented.

4.1.1 Separation of the mean and fluctuation parts

The determination of the cutoff mode M is based on three outstanding properties of the mean part: the large amount of the kinetic energy is distributed to this part; the flow fields reconstructed by M first dominant modes have a negligible cyclic variability and are highly correlated. These criteria allow two methods to distinguish the mean and fluctuation parts.

The first method profits from the standard deviation of the POD temporal coefficients permitting a cycle-to-cycle variation evaluation. At a given θ-CAD, considering the insertion depth S_k, the standard deviation of the temporal coefficients corresponding to the nth POD mode is:

$$\mathrm{std}\left(a^{(n)}(S_k)\right) = \sqrt{\frac{1}{N_t}\sum_{i=1}^{N_t}\left[\left(a^{(n)}(S_k,t_i)\right)^2 - \left(\overline{a^{(n)}(S_k)}\right)^2\right]} \tag{9}$$

where $\overline{a^{(n)}(S_k)} = \frac{1}{N_t}\sum_{i=1}^{N_t} a^{(n)}(S_k,t_i)$.

As illustrated in Fig. 5, the standard deviations of the temporal coefficients corresponding to the first two modes are more moderate than the high-order modes though the energetic differences between the POD modes are ignored. The behavior of the third mode is stated to be similar to the higher modes. Consequently, these modes are chosen as the mean part. By tabulating the POD eigenvalues, the accumulated energy of the first two modes is equal to $\lambda^{(1)} + \lambda^{(2)}$ and can be estimated superior to 75%, which confirms that the majority of the kinetic energy is attributed to the mean part. The fluctuating part owns 25% of the kinetic energy.

The second method to determine M is based on the high correlation between the velocity fields reconstructed by the modes of the mean part since this part represents the cycle-averaged flow field. For the insertion depth S_k at θ-CAD, the correlation of the velocity component $U_c^{(n_1,n_2)}$ between two snapshots taken at t_i and t_j reconstructed by the POD modes from n_1 to n_2 is calculated by the following formula:

$$R_{U_c^{(n_1,n_2)}}(t_i,t_j) = \frac{\overline{U_c^{(n_1,n_2)}(t_i)U_c^{(n_1,n_2)}(t_j)}}{\sqrt{\overline{U_c^{(n_1,n_2)}(t_i)U_c^{(n_1,n_2)}(t_i)}}\sqrt{\overline{U_c^{(n_1,n_2)}(t_j)U_c^{(n_1,n_2)}(t_j)}}} \tag{10}$$

where

$$U_c^{(n_1,n_2)}(t_i) = U_c^{(n_1,n_2)}(S_k,X_m,t_i) = \sum_{n=n_1}^{n_2} a^{(n)}(S_k,t_p)\Phi_c^{(n)}(X_m).$$

In Fig. 6, the triangle, circle and square represent S1, S2 and S3, respectively, at 90-CAD, 180-CAD and 270-CAD. The average values of the correlation coefficients of the horizontal and vertical velocity components of the whole fields are depicted by the black symbols at the top right corner of the images. In this case, all modes are utilized or $n_1 = 1$, $n_2 = N_n$ in Eq. 10.

In order to determine which modes contribute greatly to the correlation of the flow fields, we eliminate cumulatively the first modes. When mode 1 is removed or $n_1 = 2, n_2 = N_n$ are applied in the above equation, the correlation of the flow fields represented by the dark gray symbols chute greatly. In case without modes 1 and 2 ($n_1 = 3$, $n_2 = N_n$), the gray symbols show clearly the same tendency. Inversely, the removal of the first three modes or more (lighter symbols) causes only a minor change in the correlation. As a result of the flow analysis, the first two modes contribute substantially on the correlation of the total velocity fields and should be included in the mean part and $M = 2$.

For a better understanding of Fig. 6, we draw the correlation of the velocity fields of the control flap position S1 when the first modes are cumulatively eliminated in Fig. 7. Each curve corresponds to a crank angle degree 90-CAD, 180-CAD and 270-CAD. Let us consider each curve

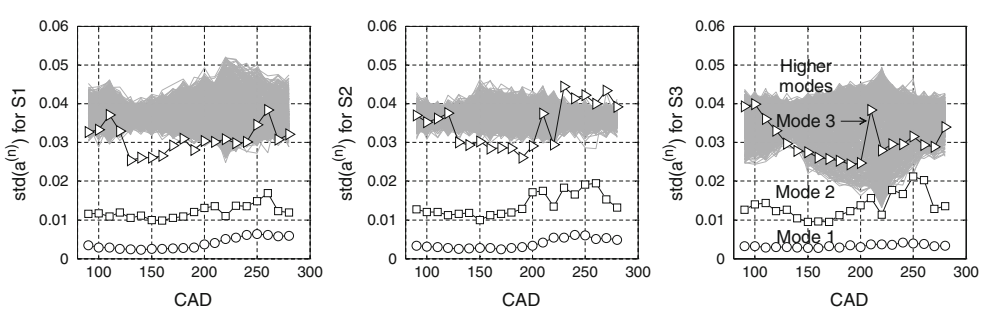

Fig. 5 Standard deviations of the temporal coefficients of mode 1 (*circle*), mode 2 (*square*), mode 3 (*triangle*) and higher modes (*gray lines*)

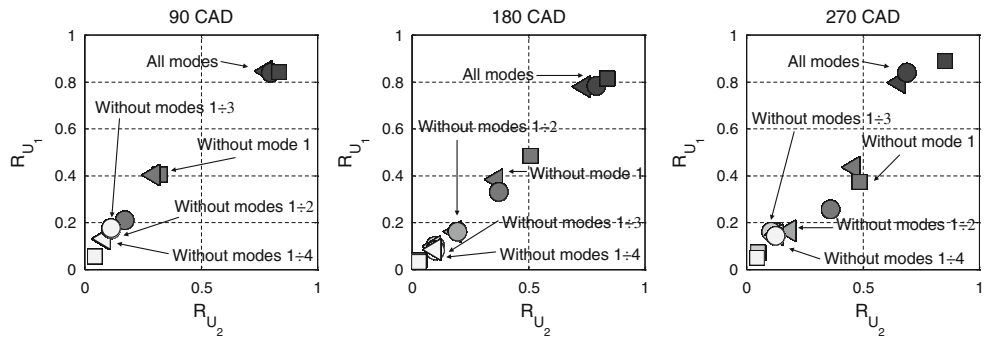

Fig. 6 Correlation of velocity fields during the accumulative removal of the first modes at 90-CAD (*left*), 180-CAD (*middle*) and 270-CAD (*right*)

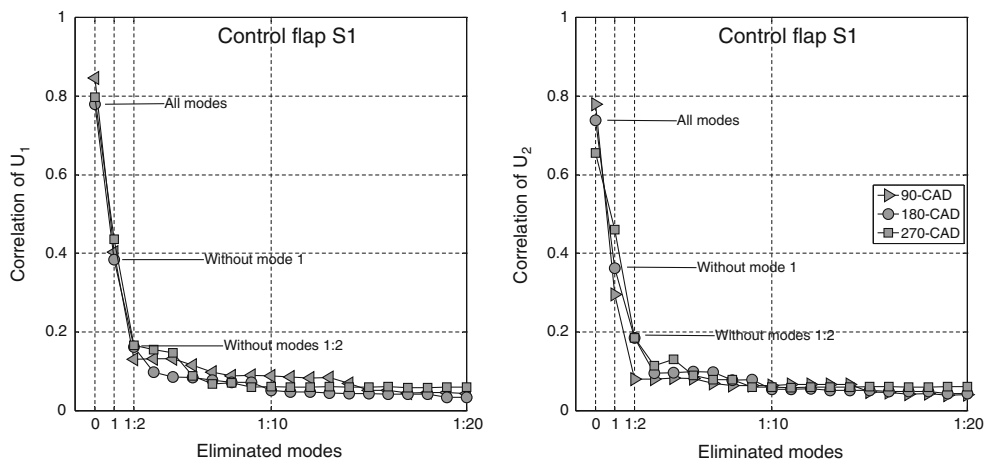

Fig. 7 Correlation of velocity fields during the accumulative removal of the first modes at 90-CAD, 180-CAD and 270-CAD for S1

(180-CAD, for example). The first point (which has a horizontal coordinate of 0) is the correlation of the velocity fields. The second point representing the correlation when mode 1 is removed has a horizontal coordinate of 1. The third point representing the correlation without modes 1 and 2 has a horizontal coordinate of 1:2. The last point (which has a horizontal coordinate of 1:20) corresponds to the correlation when first twenty modes are eliminated. One can remark easily that the correlation of the flow fields decreases substantially when the first two modes are eliminated. In contrast, the removal of the first three modes or more causes only negligible effects on the correlation.

4.1.2 Separation of the coherent and turbulent parts

The separation of the coherent and turbulent parts is a challenging task that relates to the identification of the cycle-to-cycle variations of the large-scale structures and the turbulence. One hypothesis allowing a coherent part filtering is to consider the existence of a modal boundary between the coherent part (lower modes) and a homogeneous isotropic turbulence (higher modes). This assumption has to be verified by finding a modal range given by well-known Gaussian properties of the homogeneous isotropic turbulent flows given in Pinsky et al. (2004): The skewness and flatness reach 0 and 3, respectively. Note that during the filtering process, the values of the cutoff modes will be obtained by taking into account solely the POD temporal coefficients corresponding to one insertion depth S_k at each time t_i.

$$S_{U'} = \frac{\overline{U'^3}}{\left(\overline{U'^2}\right)^{3/2}} \to 0; \quad F_{U'} = \frac{\left(\overline{U'^4}\right)^2}{\overline{U'^2}} \to 3 \tag{11}$$

where U' is the velocity component of homogeneous isotropic turbulent flows.

Supposing that the homogeneous isotropic turbulence is built by the POD modes from $C + 1$ to H, the total velocity flow in Eq. 5 becomes:

$$\begin{aligned} U(X,t) &= \underbrace{U^M(X,t)}_{\text{mean part}} + \underbrace{U^C(X,t)}_{\text{coherent part}} + \underbrace{U^T(X,t)}_{\text{turbulent part}} \\ &= \underbrace{U^M(X,t)}_{\text{mean part}} + \underbrace{U^C(X,t)}_{\text{coherent part}} + \underbrace{U^{\mathrm{IHT}}(X,t)}_{\substack{\text{isotropichomogeneous}\\ \text{turbulent part}}} \\ &+ \underbrace{U^{\mathrm{NIHT}}(X,t)}_{\substack{\text{nonisotropichomogeneous}\\ \text{turbulent part}}} \end{aligned} \tag{12}$$

with $U^{IHT}(X, t)$ reconstructed by modes from $C + 1$ to H and $U^{NIHT}(X, t)$ by modes from $H + 1$ to N_n. As shown by

the equation above, the separation of the coherent and turbulent parts would be done if one knows which POD modes contribute to the isotropic homogeneous turbulence. It is interesting to look into the evolution of the *spatial averages* of the flatness and skewness defined by the following equations as well as their *spatial standard deviations* by varying the POD modes used in the velocity field reconstruction:

$$\overline{S_{U'_c}} = \frac{1}{N_m}\sum_{m=1}^{N_m} S_{U'_c}(X_m); \quad \overline{F_{U'_c}} = \frac{1}{N_m}\sum_{m=1}^{N_m} F_{U'_c}(X_m) \tag{13}$$

and $U'_c(S_k, X_m, t_i) = \sum_{n=n_1}^{n_2} a^{(n)}(S_k, t_i)\Phi_c^{(n)}(X_m)$ velocity fields reconstructed.

In order to determine the cutoff modes of the isotropic homogeneous turbulence ($C + 1$ and H), a parametric study of $S_{U'_c}$ and $F_{U'_c}$ for two velocity components of each insertion depth at each CAD is performed by varying both n_1 and n_2 in Eq. 13. The important question is: *Which pair of* (n_1, n_2) *if it exists would guarantee the skewness and the flatness near 0 and 3, respectively*? To answer such a question, a combination of the thresholds is applied for the spatial averages and the spatial standard deviations to inform us about the relevance of the solution. The searching procedure for each control flap at a crank angle degree includes two steps, which will be resumed in the following.

Firstly, numerous cases of combining (n_1, n_2) are calculated or in other words for $n_1 = 1 \div (N_n - 1)$ and $n_2 = (n_1 + 1) \div N_n$ to deduce maps of spatial averages and of spatial standard deviations. Concretely, the first case is $n_1 = 1$, $n_2 = 2$, the second case is $n_1 = 1$, $n_2 = 3$ …, the $(N_n - 1)$ th case is $n_1 = 1$, $n_2 = N_n$ … until the last case where $n_1 = N_n - 1$, $n_2 = N_n$, is applied.

In Fig. 8, the results of the mentioned maps are shown for S3 at 270-CAD. For easy understanding of the images, let us consider a point having coordinates $n_1 = 200$; $n_2 = 600$, or in other words, $n_1 = 200$, $n_2 = 600$ are applied in Eq. 13. For example, by comparing the color level at this point with the color bar of the subplot $\overline{S_U}$, the spatial average skewness of the horizontal velocity component is roughly−0.25. Similarly, its spatial standard deviation is roughly 0.4 in the subplot rms (S_U).

Secondly, for each flap control position at a crank angle degree, we applied absolute thresholds of 0.25 for the spatial averages and 0.4 for the spatial standard deviations determined by Eq. 14 in order to choose pairs of (n_1; n_2) that are able to guarantee the skewness and the flatness near 0 and 3, respectively.

$$\begin{cases} \left|\overline{S}_{U_c^{(n_1,n_2)}} - 0\right| \le 0.25 & \mathrm{std}\left(S_{U_c^{(n_1,n_2)}}\right) \le 0.4 \\ \left|\overline{F}_{U_c^{(n_1,n_2)}} - 3\right| \le 0.25 & \mathrm{std}\left(F_{U_c^{(n_1,n_2)}}\right) \le 0.4 \end{cases} \tag{14}$$

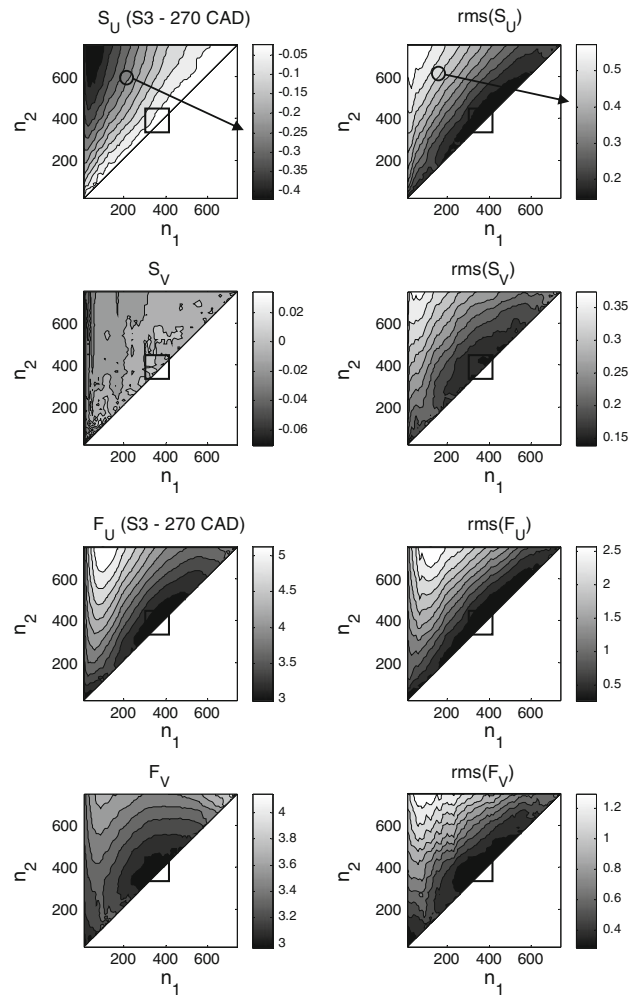

Fig. 8 Skewness (two *upper rows*) and flatness (two *lower rows*) for S3 at 270-CAD

As depicted by Fig. 8, not only a unique value but a range of pairs (n_1; n_2) satisfy the absolute thresholds of 0.25 for the spatial averages and 0.4 for the spatial standard deviations (Eq. 14). By observing the spatial standard deviation of the overall components of skewness and flatness, narrow mode windows should be chosen to pick out the isotropic homogeneous turbulence. The average modes of the ranges are finally considered as the cutoff modes of the isotropic homogeneous turbulence and are displayed by the centers having coordinates ($n_1 = C+1$; $n_2 = H$) of the black-bordered squares in Fig. 8.

In Table 2, the cutoff modes C and H separating the mean, coherent and turbulent parts are presented. These values are different depending on the insertion depths and the crank angle degrees. By tabulating the POD eigenvalues, the coherent part contains roughly 90% of the fluctuating energy and the turbulence 10%. Therefore, this energetic distribution emphasizes that the fluctuations of the flows are mostly due to the coherent part.

Table 2 Cutoff modes C and H between the mean, coherent and turbulent parts

CAD	Cutoff mode	90	100	110	120	130	140	150	160	170	180
S1	C	359	359	319	379	329	329	349	309	359	339
	H	400	410	370	430	380	370	390	350	410	390
S2	C	349	359	369	399	329	349	329	359	329	319
	H	400	410	410	450	380	390	380	410	380	370
S3	C	329	349	339	379	349	359	379	319	309	319
	H	380	390	390	420	390	400	430	360	360	370
CAD	Cutoff mode	190	200	210	220	230	240	250	260	270	280
S1	C	339	349	359	339	369	319	359	349	349	359
	H	390	410	420	400	420	360	410	400	400	410
S2	C	329	349	359	319	309	349	319	339	339	369
	H	380	400	420	370	360	400	360	390	380	410
S3	C	359	299	269	249	289	329	329	359	359	349
	H	410	350	330	290	340	370	380	400	390	390

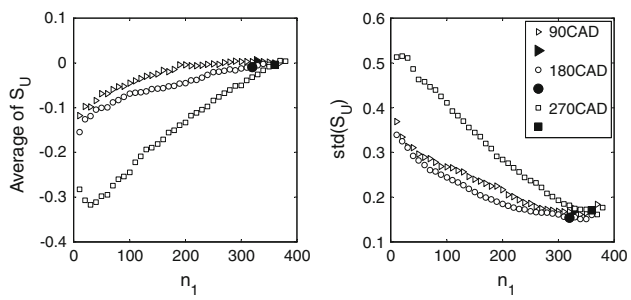

Fig. 9 *Left* average skewness of the horizontal velocity component. *Right* corresponding standard deviation (S3 at 90-CAD, 180-CAD and 270-CAD). *Filled black triangles*, *circles* and *squares* correspond to mean cutoff modes chosen

For S3 at 90-CAD, 180-CAD and 270-CAD, Fig. 9 demonstrates $\overline{S_{U_1'}}$ and its spatial standard deviation as a function of n_1 by fixing $n_2 = H$. The filled black symbols correspond to $n_1 = C + 1$. The spatial average of the skewness converge to zero (typical value of isotropic homogeneous flow) when n_1 approaches $C + 1$. Moreover, its spatial standard deviation tends to zero confirming the existence of the isotropic homogeneous turbulence within the whole fields reconstructed by the POD modes from $C + 1$ to H. Similar results were found for the flatness.

4.2 Impacts of the insertion amplitude of the control flap on the cycle-to-cycle variations

The benefit of the POD triple decomposition presented in the previous subsection is to discriminate each instantaneous snapshot into three parts. In Fig. 10, two instantaneous velocity fields taken at t_{15} and t_{150} for S3 at 180-CAD and their corresponding parts are illustrated. The mean, coherent and turbulent parts of each velocity fields are reconstructed by applying Equations 6, 7 and 8 with $M = 2$ and $C = 319$ (by referring to Table 2 for S3 at 180-CAD).

In Fig. 10, the images at first illustrate that the mean parts of two snapshots are similar over engine cycles. There are only some minor differences between the flow fields reconstructed by the first and second modes due to extremely small deviations of the corresponding POD temporal coefficients. Another possible reason is insufficient PIV snapshots. The first two modes are not statistically equal to the first moment, but they are asymptotically the mean part. Particularly, the differences remarked are in the regions where the velocity amplitudes are extremely small or even negligible. These mean parts represent therefore the temporal average flow fields. Moreover, throughout the previous section, a high correlation between the velocity fields reconstructed by the first M POD modes can be easily observed. As a result, the cyclic variability level of the mean parts is assumed to be negligible. In regard to the turbulent part, the flow fields reconstructed by the last POD modes exhibits a chaotic behavior, but in small velocity amplitudes. Additionally, this part owns a minor percentage of the fluctuating energy (10%) and therefore would not relate substantially to the cycle-to-cycle variations of the coherent structures. In particular, the coherent part contains mainly the fluctuating energy (90%) and would be the major actor of the cycle-to-cycle variations of the large-scale motions. Consequently, it is able to evaluate the cyclic variability of the engine flows to qualify influences of three insertion depths by considering only the coherent part.

In order to compare of the coherent parts owned by S1, S2 and S3, the average standard deviation of the POD

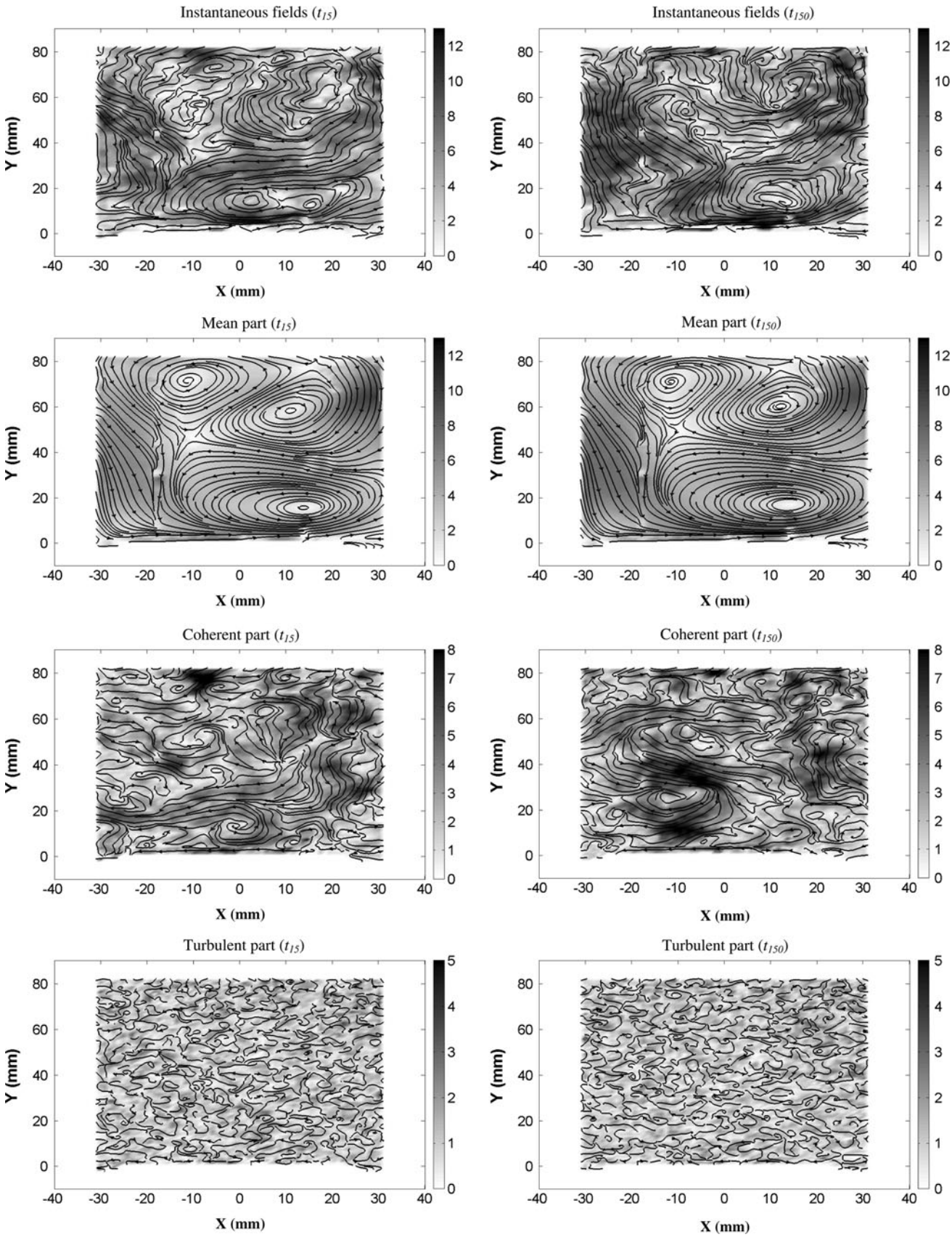

Fig. 10 Instantaneous velocity fields at t_{15} and t_{150} (S3 at 180-CAD) and the corresponding mean, coherent and turbulent parts

temporal coefficients included in the coherent part would be useful to estimate the cyclic variability level. This quantity is calculated by the following formula for the insertion depth S_k thanks to the POD-MS at θ-CAD:

$$\overline{\mathrm{std}(a_{co}(S_k,\theta))} = \frac{1}{C-M}\sum_{n=M+1}^{C}\mathrm{std}\left(a^{(n)}(S_k)\right) \tag{15}$$

where $M = 2$, and C for S_k at θ-CAD is shown in Table 2.

Our main target is to evaluate the cycle-to-cycle variations impacted by the positioning of the control flap. Figure 11 depicts the above quantity for three insertion amplitudes over the engine cycle from 90-CAD to 280-CAD. No phase information can be supplied by the POD-MS carried out independently at each CAD. The cyclic variability level of the insertion depth S3 observed is higher than the others whatever CAD. The effect of S2 is not clearly different comparing with that of S1 at the beginning of the intake stroke. In particular, the control flap placed at S1 has better role eliminating the cycle-to-cycle variations after the closing of the intake valves (210-CAD) until the start of the compression stroke (280-CAD). The moderate dispersion assured by S1 is highly expected and signify that the breaking process of the coherent structures are produced by the similar manner cycle by cycle. Consequently, coherent structure and induced turbulence intensity would be repetitively obtained, and the engine performance would be ameliorated.

In order to complete the previous results, we introduce the total kinetic energy for the flap position S_k at θ-CAD and at engine cycle t_i and its standard deviation by the following equations. Figure 12 depicts the standard deviation of the total kinetic energy (E) for three insertion depths envisaged. This quantity is pertinent to recommend the dispersion of the flow fields from one cycle to the next and to judge the previous conclusion comparing the effects of three control flap positions.

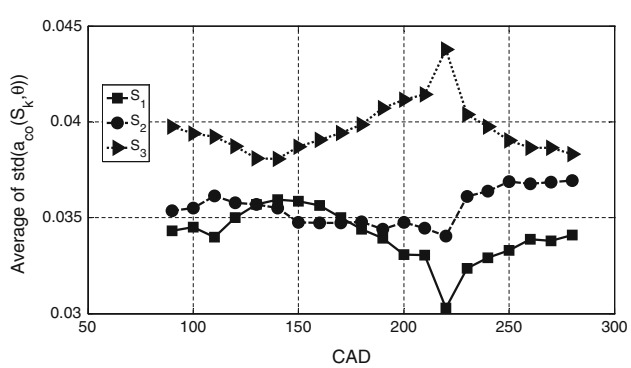

Fig. 11 Average standard deviations of the POD temporal coefficients included in the coherent parts corresponding to S1, S2 and S3

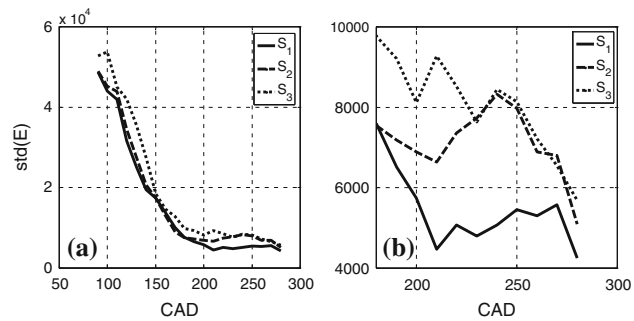

Fig. 12 *Left* standard deviation of the total kinetic energy for S1, S2 and S3. *Right* zoom in the beginning of the compression stroke

$$E(S_k,t_i) = \frac{1}{2}\sum_{m=1}^{N_m}\left|\vec{U}(S_k,X_m,t_i)\right|^2 \tag{16}$$

$$\mathrm{std}[E(S_k)] = \sqrt{\frac{1}{N_t}\sum_{i=1}^{N_t}\left[E(S_k,t_i)-\overline{E(S_k)}\right]^2} \tag{17}$$

where $\overline{E(S_k)} = \frac{1}{N_t}\sum_{i=1}^{N_t}E(S_k,t_i)$ is the cycle-averaged energy of the flow fields for S_k at θ-CAD.

As shown by the figures, the cyclic variability is significant at the beginning of the intake stroke due to the flapping of both upper and lower jets. After the closing of the intake valves (210-CAD), such flapping phenomena are stopped. After this event, there is no exterior effect except the upward movement of the piston to break the large-scale fluid motions. Thus, the cycle-to-cycle variations of the coherent structures after the closing of the intake valves have dominant influences on the turbulence-generating process. By zooming in the beginning of such process, the behavior of S2 is not clear and the engine flow exhibits large dispersions for S3. Meanwhile, the control flap positioned at S1 has a better impact stabilizing the engine flow and is expected to generate the turbulence intensity repeating cycle by cycle and therefore improve the engine efficiency. *In other words, the control flap at S1 has a better performance in terms of cycle-to-cycle variations.* These behaviors of the total kinetic energy complete the cycle-to-cycle variation analysis via POD-MS. Recently, an experimental study for three insertion amplitudes inside an SI engine with firing was carried out by Danielson Engineering, and the test results confirmed the previous conclusions.

5 Conclusions

The paper focuses on a new concept allowing in-cylinder flow control by setting a control device in the inlet pipe in order to modify the flow fields inside the combustion

chamber. It is well known that a substantial reduction in consumption could be reached as the cycle-to-cycle variations are reduced to zero. Experiments in a single transparent cylinder engine in motored conditions are proposed as to start consistency of in-cylinder flow properties controlled by introducing a small control instrument and expecting non-negligible impacts.

At each CAD, all the velocity fields given by three insertion amplitudes have been concatenated using a proper orthogonal decomposition as to obtain a unique eigenfunction database. This allows, according to a velocity mean square (kinetic energy) projection, a selection of cutting mode for isolating the coherent component of the flow by extracting the mean and turbulent parts.

The POD analysis filtering indicates that the mean flow can be described by the first two POD modes according to low root mean square of the corresponding temporal coefficients as well as high correlation level of the mean part. To discriminate the coherent part of the flow, the cutoff mode choice is obtained by the evaluation of the skewness and the flatness (3rd- and 4th-centered statistical moments). After filtering the velocity field, the results indicate that the coherent part reaches roughly 90% of the fluctuating kinetic energy and the turbulence 10%. In other words, the cycle-to-cycle variations are mostly due to the coherent part.

A coefficient describing the cycle-to-cycle variations is also introduced by averaging the standard deviation of the POD temporal coefficients corresponding to the coherent part. The flow steadiness is mainly impacted by the coherent part generating the discrepancies of the large-scale structures from one cycle to the next. This coefficient permits to compare results obtained by different insertion amplitudes.

As a general conclusion, the modification of the intake pipe geometry by placing a control flap near the intake valve shows one major consequence: the cycle-to-cycle variations of the fluid structures are modified depending on the insertion of the control device. The paper defines an original approach in order to manage a better optimization of the in-cylinder flow properties by minimizing the insertion amplitude in order to avoid the dispersions over the engine cycles and especially the cycle-to-cycle variations of the coherent fluid structures and their breaking process. The method proposed is considered valuable up to the beginning of the compression stroke at roughly 280-CAD.

Acknowledgments The authors would like to gratefully acknowledge Mr. Jérôme Bonnéty for supports on experimental study and helpful discussions during the database post-treatment. This work was performed on behalf of the PREDIT program named OPERA and supported by Danielson Engineering, PSA and the French agency ADEME.

References

Berkooz G (1991) Turbulence, coherent structures and low dimensional models. Cornell University, Ithaca, NY

Berkooz G, Holmes PJ, Lumley JL (1993) The proper orthogonal decomposition in the analysis of turbulent flows. Annu Rev Fluid Mech 25:539–575

Bizon K, Continillo G, Mancaruso E, Merola SS, Vaglieco BM (2010) POD-based analysis of combustion images in optically accessible engines. Combust Flame 157(4):632–640

Brown GL, Roshko A (1974) On density effects and large structures in turbulent mixing layers. J Fluid Mech 64:775–816

Cosadia I, Borée J, Charnay G, Dumont P (2006) Cyclic variations of the swirling flow in a diesel transparent engine. Exp Fluids 41(1):115–134

Druault P, Chaillou C (2007) Use of proper orthogonal decomposition for reconstructing the 3D in-cylinder mean-flow field from PIV data. Comptes Rendus Mécanique 335(1):42–47

Druault P, Guibert P, Alizon F (2005a) Use of proper orthogonal decomposition for time interpolation from PIV data—application to the cycle-to-cycle variation analysis of in-cylinder engine flows. Exp Fluids 39(6):1009–1023

Druault P, Delville J, Bonnet JP (2005b) Proper orthogonal decomposition of the mixing layer flow into coherent structures and turbulent Gaussian fluctuations. Comptes Rendus Mécanique 333(11):824–829

Eichenberger DA, Robert WL (1999) Effect of unsteady stretch on spark ignited flame kernel survival. Combust Flame 118(3): 469–478

Enotiadis AC, Vafidis C, Whitelaw JH (1990) Interpretation of cyclic flow variations in motored internal combustion engines. Exp Fluids 10(2–3):77–86

Epureanu BI (2003) A parametric analysis of reduced order models of viscous flows in turbomachinery. J Fluids Struct 17(7):971–982

Fansler TD (1993) Turbulence production and relaxation in bowl-in-piston engines, SAE technical paper 930479

Floch A, Van Frank J, Ahmed A (1995) Comparison of the effects of intake generated swirl and tumble on turbulence characteristics in a four-valve engine. SAE Transact 104(3):2239–2255

Fogleman M, Lumley J, Rempfer D, Haworth D (2004) Application of the proper orthogonal decomposition to datasets of internal combustion engine flows. J Turbul 5:1–18

Graftieaux L, Michard M, Grosjean N (2001) Combining PIV, POD and vortex identification algorithms for the study of unsteady turbulent swirling flows. Meas Sci Technol 12(9):1422–1429

Guibert P, Le Moyne L (2002) Dual particle image velocimetry for transient flow field measurements. Exp Fluids 33(2):355–367

Han Z, Reitz RD (1995) Turbulence modeling of internal combustion engines using RNG I–I models. Combust Sci Technol 106(4–6): 267–295

Heywood JB (1988) Internal combustion engine fundamental. McGraw-Hill, NY

Holmes PJ, Berkooz G, Lumley JL (1998) Turbulence, coherent structures, dynamical systems and symmetry. Cambridge University Press, Cambridge, MA

Huang RF, Yang HS, Yeh CN (2008) In-cylinder flows of a motored four-stroke engine with flat-crown and slightly concave-crown pistons. Exp Thermal Fluid Sci 32(5):1156–1167

Huang RF, Lin KH, Yeh CN, Lan J (2009) In-cylinder tumble flows and performance of a motorcycle engine with circular and elliptic intake ports. Exp Fluids 46(1):165–179

Hussain AKMF (1986) Coherent structures and turbulence. J Fluid Mech 173:303–356

Isaka Y, Higaki Y (1995) Development of Yamaha tumble induction control system (YTIS), SAE technical paper 950201

Jebamani DR, Kumar TMN (2008) Studies on variable swirl intake system for DI diesel engine using computational fluid dynamics. Thermal Sci 12(1):25–32

Kuwahara K, Ando H (2000) Diagnostics of in-cylinder flow, mixing and combustion in gasoline engine. Meas Sci Technol 11(6):95–111

Lenglet F (2006) Moteur à combustion interne avec Moyens de Giration du Fluide d'Admission, Bulletin officiel de la Propriété Industrielle, INPI, FR2909716(A1). Website: http://fr.espacenet.com

Lumley JL (1967) The structure of inhomogeneous turbulent flows. In proceedings of the international colloquium, pp 166–178

Ly HV, Tran HT (2001) Modeling and control of physical processes using POD. Math Comput Model 33(1–3):223–236

Matekunas FA (1983) Modes and measures of cyclic combustion variability. SAE Trans 92(1):1139–1156

Perret L, Collin E, Delville J (2006) Polynomial identification of POD based low-order dynamical system. J Turbul 7(17):1–15

Pinsky M, Shapiro M, Khain A, Wirzberger H (2004) A statistical model of strains in homogeneous and isotropic turbulen. Physica D-Nonlinear Phenom 191:297–313

Ravindran SS (2002) Control of flow separation over a forward-facing step by model reduction. Comput Methods Appl Mech Eng 191(41–42):4599–4617

Reeves M, Garner CP, Dent JC, Halliwell NA (1994) Particle image velocimetry measurements of Barrel Swirl in a production geometry optical IC engine, SAE technical paper 940281, pp 1–9

Reeves M, Garner CP, Dent JC, Halliwell NA (1996) Full-field ic engine flow measurement using PIV. Optical Eng 35(2):579–587

Reeves M, Towers DP, Tavender B, Buckberry CH (1999) A high-speed all-digital technique for cycle-resolved 2-D flow measurement and flow visualisation within SI engine cylinders. Optics and Lasers in Eng 31(4):247–261

Rempfer D, Fasel HF (1994) Evolution of three-dimensional coherent structures in a flat-plate boundary layer. J Fluid Mech 260:351–375

Reuss DL, Andrian RJ, Landreth CC, French DT, Fansler TD (1989) Instantaneous planar measurements of velocity and large scale vorticity and strain rate in an engine using particle image velocimetry, SAE technical paper 890616

Roudnitzky S, Druault P, Guibert P (2006) Proper orthogonal decomposition of In-cylinder engine flow into mean component, coherent structures and random Gaussian fluctuations. J Turbul 7(70):1–19

Rowley CW, Colonius T, Murray RM (2004) Model reduction for compressible flows using POD and Galerkin projection. Physica D: Nonlinear Phenom 189(1–2):115–129

Sirovich L (1987) Turbulence and dynamics of coherent structures. Q Appl Math 45(3):561–571

Stansfield P, Wigley G, Justham T, Catto J, Pitcher G (2007) PIV analysis of in-cylinder flow structures over a range of realistic engine speeds. Exp Fluids 43(1):135–146

Tabaczinski RJ (1990) Turbulent flows in reciprocating internal combustion engines. Internal combustion engine technology, Elsevier Science Publishers, Amsterdam, pp 243–285

Towers DP, Towers CE (2004) Cyclic variability measurements of in-cylinder engine flows using high speed particle image velocimetry. Meas Sci Technol 15(9):1917–1925

Utturkar Y, Zhang B, Shyy W (2005) Reduced-order description of fluid flow with moving boundaries by proper orthogonal decomposition. Int J Heat Fluid Flow 26(2):276–288

Westerweel J (1997) Fundamentals of digital particle image velocimetry. Meas Sci Technol 8(12):1379–1392

Young MB (1981) Cyclic dispersion in the HCCI engine—a literature survey, SAE technical paper 810020

Zhongchang L, Xunjun L, Zhaohe Z (2002) Reducing exhaust emissions from an automotive DI diesel engine by means of air injection variable swirl inlet system, presented at the proceedings of the IEEE international vehicle electronics conference